

Synthetic Control of the Photoluminescence Stability of Organolead Halide Perovskites

Daniel J. Freppon,^{1,2} Long Men,^{1,2} Ujjal Bhattacharjee,^{1,2} Bryan A. Rosales,¹ Feng Zhu,¹ Jacob W. Petrich,^{1,2} Emily A. Smith,^{*1,2} and Javier Vela^{*1,2}

¹Department of Chemistry, Iowa State University.

²Ames Laboratory, Ames, Iowa 50011.

*Corresponding author: Emily A. Smith, e-mail: esmith1@iastate.edu; Javier Vela, e-mail: vela@iastate.edu

Received July 7th, 2018; Accepted April 9th, 2019.

DOI: <http://dx.doi.org/10.29356/jmcs.v63i3.623>

Abstract. An optimized synthetic procedure for preparing photostable nanocrystalline methylammonium lead halide materials is reported. The procedure was developed by adjusting the lead halide to methylammonium/octylammonium halide precursor ratio. At a high precursor ratio (1:3), a blue-shifted photoinduced luminescence peak is measured at 642 nm for CH₃NH₃PbI₃ with 0.01 to 12 mJ pulsed-laser irradiation. The appearance of this peak is reversible over 300 min upon blocking the irradiation. In order to determine if the peak is the result of a phase change, *in situ* x-ray diffraction measurements were performed. No phase change was measured with an irradiance that causes the appearance of the photoinduced luminescence peak. Luminescence microspectroscopy measurements showed that the use of a lower precursor ratio (1:1.5) produces CH₃NH₃PbI₃ and CH₃NH₃PbBr₃ perovskites that are stable over 4 min of illumination. Given the lack of a measured phase change, and the dependence on the precursor ratio, the photoinduced luminescence peak may derive from surface trap states. The enhanced photostability of the resulting perovskite nanocrystals produced with the optimized synthetic procedure supports their use in stable optoelectronic devices.

Keywords: surface traps, nanocrystalline perovskites, photostability, single nanocrystal analysis, synthetic optimization, optoelectronics.

Resumen. Se reporta un proceso sintético optimizado para preparar materiales haluros de metilamonio-plomo nanocristalinos fotoestables. El proceso fue desarrollado ajustando la relación entre los precursores de haluro de metilamonio y haluro de octilamonio. Con una relación de precursores alta (1:3), un pico luminiscente desviado al azul a 642 nm fue detectado para CH₃NH₃PbI₃ con irradiación de láser de pulso entre 0.01 y 12 mJ. La aparición de éste pico es reversible hasta por 300 min después de cesar la irradiación. Para determinar si éste pico se debe a una transición de fase, se hicieron mediciones de difracción de rayos-X *in situ*. Ningún cambio de fase fue detectado con niveles de irradiación a los cuales se observa el pico luminiscente. Mediciones luminiscentes macrospectroscópicas muestran que con una relación de precursores más baja (1:1.5) se producen perovskitas CH₃NH₃PbI₃ y CH₃NH₃PbBr₃ que son estables hasta con 4 min de iluminación. Dado que no se observa un cambio de fase, y la dependencia sobre la relación de precursores, el pico luminiscente generado bajo iluminación podría derivarse de estados trampa de superficie. La fotoestabilidad incrementada de los nanocristales de perovskita obtenidos por el procedimiento sintético optimizado ayudan a su aplicación en dispositivos optoelectrónicos más estables.

Palabras clave: trampas de superficie, perovskitas nanocristalinas, fotoestabilidad, análisis de nanocristal individual, optimización sintética, optoelectrónica

Introduction

Organolead halide perovskite semiconductors of general composition RPbX_3 (R = organic monocation, such as CH_3NH_3^+ ; X = halide, such as I or Br) have drawn attention as both photovoltaic [1, 2] and optoelectronic [3] materials. Broad light absorption and long carrier diffusion lengths make perovskites ideal light harvesters [4]. The certified power conversion efficiency of perovskite solar cells surged from 3.8% to over 22% in the last 8 years [5-10]. In spite of these many advantages, organometal halide perovskites suffer from instability against moisture, heat and light [11-13]. A deeper understanding of the fundamental physical and chemical behavior of perovskites could help in mitigating these instability issues, thus enabling their implementation and deployment into many energy technologies [14, 15].

Efforts to improve the physical and chemical properties of perovskites have focused primarily on tuning their composition or dimensionality [16, 17]. Compositional and dimensional control are useful in tuning the bandgap energies of some perovskite materials [18, 19]. Partial substitution with long alkylammonium cations leads to low dimensional perovskites [20-22], some of which exhibit enhanced moisture stability. Control of optoelectronic properties through mixing cations and halides has been widely exploited in enhancing the power conversion efficiency of perovskite solar cells [14, 23-25]. Compositional variants of halide perovskites have bandgap and luminescence energies that cover the entire visible spectrum [9, 26-28]. Halide substitution also leads to enhanced stability, as $\text{CH}_3\text{NH}_3\text{PbI}_3$ solar cells doped with Br show long-lasting resistance against humidity [29, 30]. $\text{CH}_3\text{NH}_3\text{PbBr}_3$ displays lower sensitivity to concentrated sunlight compared to $\text{CH}_3\text{NH}_3\text{PbI}_3$ [31].

A few reports describe the unusual photophysical behavior of organometal halide perovskites, specifically a reversible shift in photoluminescence maximum (λ_{max}) under thermal and photochemical conditions [32-34]. Gottesman *et al.* observed a decrease in luminescence intensity and increase in the 108 cm^{-1} Raman band of $\text{CH}_3\text{NH}_3\text{PbI}_3$ solar cells, and attributed these changes to slow photoinduced structural changes since the timescale of the change was not consistent with an electronic process [34]. Sadhanala and co-workers measured two absorption peaks in freshly-prepared, mixed-halide $\text{CH}_3\text{NH}_3\text{Pb}(\text{Br}_{1-x}\text{I}_x)_3$ perovskite films. A single absorption band, however, was measured after aging the film for 21 days [33]. Hoke *et al.* have also reported light-induced changes to the absorption and photoluminescence spectra of $\text{CH}_3\text{NH}_3\text{Pb}(\text{Br}_{1-x}\text{I}_x)_3$ perovskite films. They attribute these behaviors to reversible crystalline changes and trap states [32]. Structural defects and ion migration contribute to the notorious photocurrent hysteresis [35, 36] and specific quantum efficiency [37] that characterizes perovskite semiconductors and devices. Unusual photophysics that are caused by surface defects may become even more prominent in nanocrystalline perovskites [38].

Trap states in perovskites. $\text{CH}_3\text{NH}_3\text{PbI}_3$ has a broad emission band and a high quantum yield of photoluminescence. The nature of the radiative decay channels and the spectral broadening mechanisms are largely determined by phonon coupling effects and defects or trap states [39]. Trap states are likely to occur at the surface of perovskite nanocrystals [38]. Vacancies, such as ionic defects like Pb^+ , I, and CH_3NH_3^+ , can also form shallow trap states and reduce carrier lifetimes [40]. Strong covalency of the Pb cations and I anions lead to the formation of Pb dimers and iodide trimers, which are responsible for transition levels that can serve as recombination centers that reduce solar-cell performance [41]. Trap states increase the frequency of non-radiative recombination, which reduces the quantum yield [42]. Density-functional theory studies have revealed the unusual defect physics of $\text{CH}_3\text{NH}_3\text{PbX}_3$ [41, 43-46]. For example, shallow point defects could explain in part the ultra-high open-circuit voltages of $\text{CH}_3\text{NH}_3\text{PbBr}_3$ solar cells [46].

Synthetic conditions play an important role in the formation of trap states. For example, perovskites grown under high iodine concentrations are likely to have defects (lead atom substituted by iodide) and a high density of deep electronic traps (recombination centers) that cause short diffusion lengths and poor photovoltaic performance [47]. Supramolecular halogen bond complexation can passivate the under-coordinated iodine ions, which can reduce trap sites near the perovskite surface [48]. Lewis bases are used to passivate under-coordinated lead atoms, and treated perovskites exhibited reduced electron-hole recombination and consequently longer photoluminescence lifetimes [49]. Adding fullerene layers has also proven to be an effective way to passivate the charge trap states and get rid of photocurrent hysteresis [35, 50].

Building on our previous work [22], a systematic synthesis of photostable nanocrystalline $\text{CH}_3\text{NH}_3\text{PbX}_3$ is demonstrated. Optimization of the $\text{CH}_3\text{NH}_3\text{PbI}_3$ alkyl halide to lead halide precursor ratio,

inhibited the appearance of a reversible photoinduced 630-nm photoluminescence peak that may be derived from surface traps. Using an optimized synthetic procedure, luminescence of single $\text{CH}_3\text{NH}_3\text{PbI}_3$ and $\text{CH}_3\text{NH}_3\text{PbBr}_3$ nanocrystals was stable over 240 seconds with over $1 \times 10^5 \text{ W/cm}^2$ irradiance. The reported optimized synthesis may be applicable to other organometal halide perovskites, for example those with mixed halide composition.

Experimental

Materials

Lead(II) bromide ($\geq 98\%$), N,N-dimethylformamide (DMF), lead(II) iodide (99%), methylamine (33 wt% in ethanol), *n*-octylamine (99%), and toluene (anhydrous, 99.8%) were purchased from Sigma-Aldrich. Hydrobromic acid (ACS, 47.0-49.0%), hydroiodic acid (ACS, 55-58%), and oleic acid (tech., 90%) from Alfa-Aesar; diethyl ether from Baker; toluene (99.9%) and acetonitrile (99.9%) from Fisher. Materials were used as received unless specified otherwise.

Synthesis

Ammonium Halides. Dimensionality control is achieved using a bulky alkylammonium cation as a capping ligand. Hydrogen halides were prepared by a modified literature procedure [45]. Briefly, hydroiodic acid (10 mL, 0.075 mol) or hydrobromic acid (8.6 mL, 0.075 mol) was added to a solution of excess methylamine (24 mL, 0.192 mol) in ethanol (100 mL) at 0 °C, and the mixture stirred at this temperature for 2 h. The sample was concentrated under vacuum, and the resulting powder dried under dynamic vacuum at 60 °C for 12 h and recrystallized from ethanol. Both *n*-octylammonium iodide ($\text{CH}_3(\text{CH}_2)_7\text{NH}_3\text{I}$) and *n*-octylammonium bromide ($\text{CH}_3(\text{CH}_2)_7\text{NH}_3\text{Br}$) were washed repeatedly with diethyl ether and dried under dynamic vacuum before use.

Nanocrystalline $\text{CH}_3\text{NH}_3\text{PbX}_3$. PbX_2 (0.008 mmol), $\text{CH}_3\text{NH}_3\text{X}$ (0.012 mmol) and $\text{CH}_3(\text{CH}_2)_7\text{NH}_3\text{X}$ (0.012 mmol) were dissolved in a mixture of acetonitrile (20 mL) and DMF (200 μL). 4 mL of the resulting precursor solution was rapidly injected into toluene (15 mL) while stirring. After 24 h stirring at 20 °C, solids were isolated by centrifugation (10 min at 4000 rpm) and purified by washing with toluene (5 mL) followed by re-centrifugation.

Structural Characterization

X-ray diffraction (XRD) was collected on a Rigaku Ultima IV (40 kV, 44 mA). A Cu KR source was used for radiation. A quartz sample holder was used as a substrate for drop-casted toluene solvated samples. Details of the in situ measurements were as previously reported [51]. Transmission Electron Microscopy (TEM) images were collected using a FEI Tecnai G2 F20 field-emission TEM capable of 200 kV with a point-to-point resolution of less than 0.25 nm having a 0.10-nm line-to-line resolution. Dilute solutions were prepared in toluene and 2 to 3 drops of each product were placed onto carbon-coated copper grids. TEM images were used to measure the particle dimensions and were processed using the ImageJ program. Typically, more than 100 particles were counted in each case. Uncertainties in all measurements are reported as standard deviations.

Optical Characterization

Solution-phase optical extinction (absorption plus scattering) spectra were collected using an Agilent 8453 UV/Vis spectrophotometer equipped with a photodiode array. Solvent absorption was subtracted from all spectra. Drop-casted solid films of each sample were measured using diffuse reflectance (SL1 Tungsten Halogen lamp (vis-IR), a SL3 Deuterium Lamp (UV), and a BLACK-Comet C-SR-100 Spectrometer). A Horiba-Jobin Yvon Nanolog scanning spectrofluorometer equipped with a photomultiplier detector was used to collect steady-state PL spectra. Quantum yields for each nanocrystalline perovskite were calculated by comparing luminescence intensities of Rhodamine 590 or 640 [52].

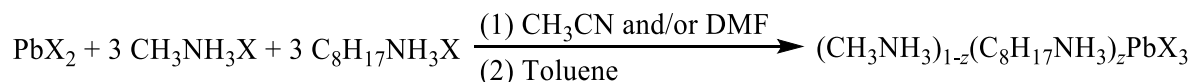
For the luminescence microspectroscopy of single nanocrystals, a DM IRBE microscope (Leica, Wetzlar, Germany) was employed. Monochromatic illumination with a 532 nm laser (Coherent, Santa Clara,

CA) was used to excite $\text{CH}_3\text{NH}_3\text{PbI}_3$, and a 488 nm Argon ion laser (Uniphase, San Jose, CA) for $\text{CH}_3\text{NH}_3\text{PbBr}_3$. An oil-immersion objective producing a spot with a $0.28 \pm 0.03 \mu\text{m}$ diameter provided an excitation power density of $1.6 \times 10^5 \text{ W}\cdot\text{cm}^{-2}$. PL was collected using a HoloSpec f/1.8i spectrograph (Kaiser Optical Systems, Ann Arbor, MI, USA) equipped with a broad-range grating (HFG-650, Kaiser Optical Systems) and a charged-coupled device (CCD) (Newton 940, Andor Technology, Belfast, UK) with a collection binning time of 0.05 s. 2400 spectra were collected every 0.09873 seconds.

Results and discussion

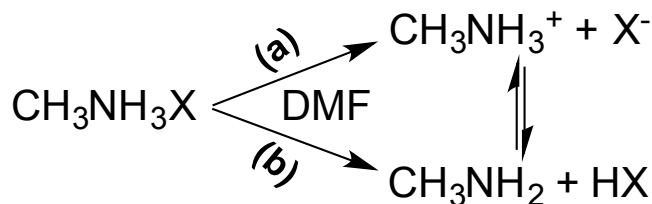
General Synthesis and Characterization

Nanocrystalline organolead halide perovskites are prepared by dissolving (a) PbX_2 , (b) $\text{CH}_3\text{NH}_3\text{X}$, and (c) $\text{CH}_3(\text{CH}_2)_7\text{NH}_3\text{X}$ ($\text{X} = \text{I}$ or Br) precursors in a polar solvent such as dimethyl formamide (DMF, $\epsilon = 38.25$) or acetonitrile ($\epsilon = 36.64$), followed by quick injection into a less polar solvent such as toluene ($\epsilon = 2.379$) as shown in Scheme 1 [22]. DMF, acetonitrile, or both are used because they provide excellent precursor solubility, as we reported previously for the synthesis of perovskite nanowires [22]. Introduction of a large ionic ligand, such as an ammonium or carboxylate-containing surfactant, decreases the perovskite particle size. In this study, the concentration of the $\text{CH}_3\text{NH}_3\text{X}$ and larger alkyl ammonium halide, $n\text{-CH}_3(\text{CH}_2)_7\text{NH}_3\text{X}$, are equivalent. In this way low-dimensional nanocrystalline perovskites are synthesized [16, 38, 53]. Perovskite nanocrystals produced by this method contain methyl ammonium cations within their core, and octyl ammonium groups on their surface [54].



Scheme 1. Synthesis of nanocrystalline organolead halide ($\text{X} = \text{Br}$ or I) perovskites prepared using a molar concentration of alkylammonium halide precursor that is $3\times$ higher than that of the lead halide precursor; $0 < z \ll 1$.

During the synthesis of iodide perovskites, the PbI_2 precursor fails to dissolve completely in the co-solvent unless an excess of ammonium halide precursors is present. A very large excess of ammonium halides, however, irreversibly affects the optical properties of the resulting perovskites, as discussed below. Precursor reactivities and ease of forming solid solutions also affect the product. $\text{CH}_3\text{NH}_3\text{X}$ salts dissociate differently in DMF depending on the specific halide (Scheme 2). For iodide, the preferred products are CH_3NH_3^+ and I^- , the conjugate base of HI , which is a strong acid in DMF and leads to a large conductivity (Scheme 2, Fig. 1 when $[\text{PbX}_2]_0 = 0$). For bromide the preferred products are CH_3NH_2 along with HBr , which is a weaker acid in DMF and leads to a smaller conductivity (Scheme 2, Fig. 1 when $[\text{PbX}_2]_0 = 0$). Thus, $\text{CH}_3\text{NH}_3\text{I}$ is expected to be the most reactive ammonium halide precursor in DMF, generating free and readily available I^- needed for perovskite formation that should be easily precipitated upon addition of a nonpolar solvent such as toluene.



Scheme 2. Pathways of $\text{CH}_3\text{NH}_3\text{X}$ dissociation in DMF.

To probe PbX_2 precursor reactivity, we measured their specific conductivities (κ) in DMF with both the presence and absence of a set amount of the corresponding $\text{CH}_3\text{NH}_3\text{X}$ (Fig. 1). As expected, in pure DMF, the conductivity increases linearly with PbX_2 concentration. Conductivity is proportional to the number of ions in solution, thus enabling a comparison to the relative degree of dissociation and association. A steeper increase for the iodide case suggests that dissociation is slightly higher for PbI_2 than for PbBr_2 . With the presence of 50 mM $\text{CH}_3\text{NH}_3\text{X}$ in DMF, the conductivity actually decreases upon addition of PbI_2 and slowly increases upon addition of PbBr_2 . When a 1 to 3 ratio of PbX_2 to $\text{CH}_3\text{NH}_3\text{X}$ is used, as is the case in the Scheme 1 perovskites, the conductivity is higher for $\text{PbI}_2/\text{CH}_3\text{NH}_3\text{I}$ than $\text{PbBr}_2/\text{CH}_3\text{NH}_3\text{Br}$ suggesting that Pb-Br binding in solution is stronger than Pb-I binding. A similar observation was reported by luminescence and transient absorption measurements [55].

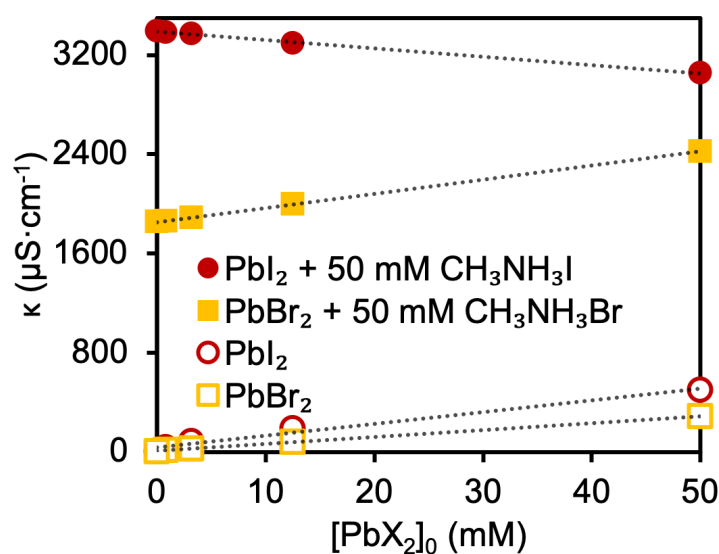


Fig. 1. Specific conductivity (κ) vs. PbX_2 concentration with (solid) or without (hollow) 50 mM $\text{CH}_3\text{NH}_3\text{X}$.

Structural Analysis

Powder X-ray diffraction (XRD) patterns show the diffraction peaks corresponding to the $\langle 110 \rangle$ and $\langle 001 \rangle$ facets of the $\text{CH}_3\text{NH}_3\text{PbI}_3$ and $\text{CH}_3\text{NH}_3\text{PbBr}_3$ nanocrystals (Fig. 2). $\text{CH}_3\text{NH}_3\text{PbBr}_3$ shifts to higher 2θ values since bromine has a higher electronegativity compared to iodine, indicating some degree of solid solution, consistent with literature [56, 57]. Table 1 presents the lattice parameter of cubic $\text{CH}_3\text{NH}_3\text{PbBr}_3$ and tetragonal $\text{CH}_3\text{NH}_3\text{PbI}_3$ nanocrystalline perovskites as determined experimentally from XRD analysis.

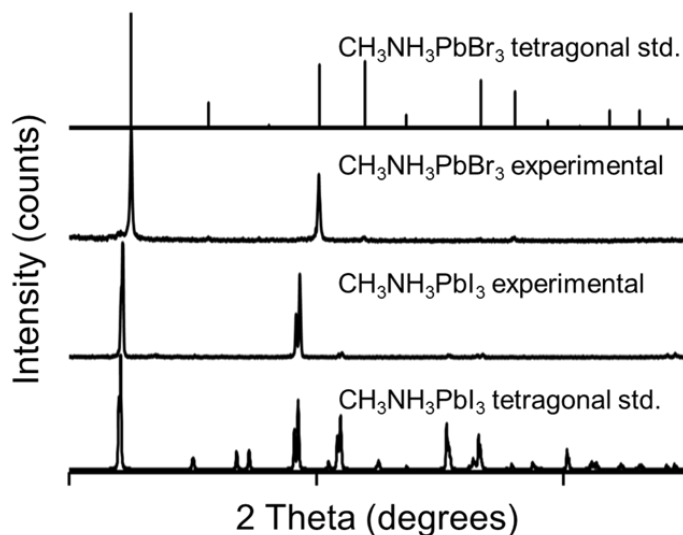


Fig. 2. Powder XRD of nanocrystalline organometal halide perovskites with corresponding standard (std.) diffraction patterns.

The transmission electron microscopy (TEM) images shown in Fig. 3 reveal that the perovskites are primarily nanospheres with an average size of 7 ± 2 nm for $\text{CH}_3\text{NH}_3\text{PbI}_3$ and 8 ± 2 nm for $\text{CH}_3\text{NH}_3\text{PbBr}_3$. The Bohr radii for bromide and iodide perovskites are 2 and 2.2 nm, respectively [58]. In addition to the nanospheres, the $\text{CH}_3\text{NH}_3\text{PbBr}_3$ perovskites exhibit nanosheets making up *ca.* 10-20% of the total particles. As we previously reported, perovskite nanosheets are unstable under the TEM electron beam [22]. The presence of nanosheets is a contributing factor for the preferred orientation behavior observed by powder XRD for $\text{CH}_3\text{NH}_3\text{PbI}_3$ perovskite nanocrystals.

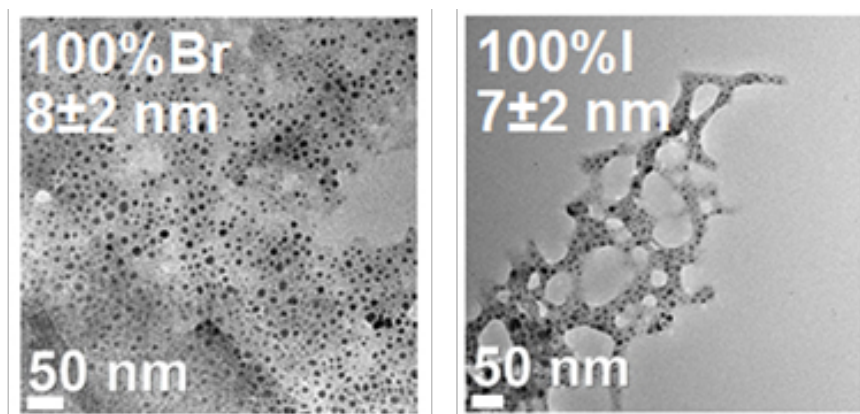


Fig. 3. Representative TEM images of $\text{CH}_3\text{NH}_3\text{PbBr}_3$ and $\text{CH}_3\text{NH}_3\text{PbI}_3$ nanocrystalline perovskites.

Optical Properties and Photostability

Using a spectrofluorometer with arc lamp illumination, the λ_{max} for $\text{CH}_3\text{NH}_3\text{PbI}_3$ was determined to be 760 nm; and that for $\text{CH}_3\text{NH}_3\text{PbBr}_3$, 518 nm. This is consistent with literature reports for perovskites of similar composition [59-61]. The $\text{CH}_3\text{NH}_3\text{PbBr}_3$ perovskite sample has a 29-fold higher photoluminescence quantum yield (44%) compared to $\text{CH}_3\text{NH}_3\text{PbI}_3$ (Table 1).

Table 1. Characterization parameters of low-dimensional organometal halide perovskites.

Loading	a ¹ (nm)	Scherrer Size (nm)	TEM ² Size (nm)	Abs. Edge (nm)	Band Gap (eV)	First-Exciton Luminescence (nm)	Quantum Yield (%)
CH ₃ NH ₃ PbBr ₃	0.587	7	8±2	527	2.35	506	44
CH ₃ NH ₃ PbI ₃	0.634	>100	7±2	774	1.60	745	1.5

¹Lattice parameter (a). ²More than 100 nanocrystals measured.

Nanocrystalline perovskites prepared using Scheme 1 with an a:b:c precursor ratio of 1:3:3 exhibited two luminescence peaks in a flash photolysis experiment with nanosecond pulsed Nd:YAG laser illumination. One peak had a λ_{\max} at 745 nm (E_g) and the second peak had a λ_{\max} at 642 nm ($E > E_g$) for CH₃NH₃PbI₃ and 0.01 mJ pulsed-laser illumination (Fig. 4a). With increasing excitation energy the relative intensity of the 642 nm peak increases nonlinearly (Fig. 4b) and both peaks blue shift. With 12 mJ illumination, the λ_{\max} are 626 nm and 725 nm.

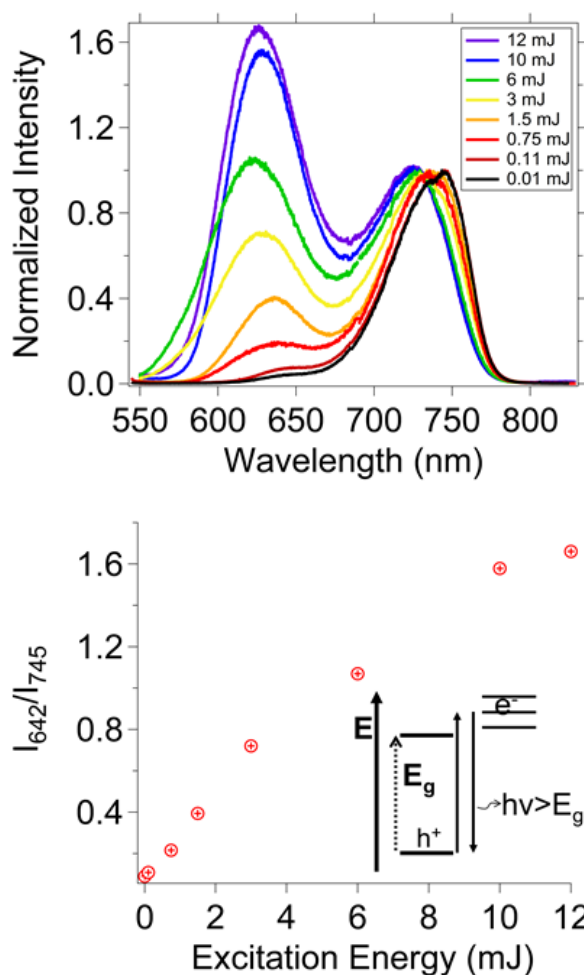


Fig. 4. (Top) Flash photolysis luminescence spectra of nanocrystalline CH₃NH₃PbI₃, prepared using Scheme 1, as a function of excitation power. The spectra are normalized to the intensity at ~745 nm (at the λ_{\max}). **(Bottom)** Intensity ratios of the ~642 nm (I_{642}) and ~745 nm (I_{745}) bands vs. incident laser power. The inset explains the band gap (E_g) of the nanocrystalline perovskite “vs” the higher energy trap state luminescence.

To determine if the photoinitiated increase in the 642 nm peak intensity was reversible, the luminescence spectrum of the $\text{CH}_3\text{NH}_3\text{PbI}_3$ nanocrystals was monitored in a new-batch of nanocrystals after blocking the laser irradiation. After 300 minutes in the dark, the intensity of the band at 642 nm decreased due to a thermal relaxation mechanism. The photoinitiated reversible spectral changes may be the result of changes in the crystal phase or the population of surface traps.

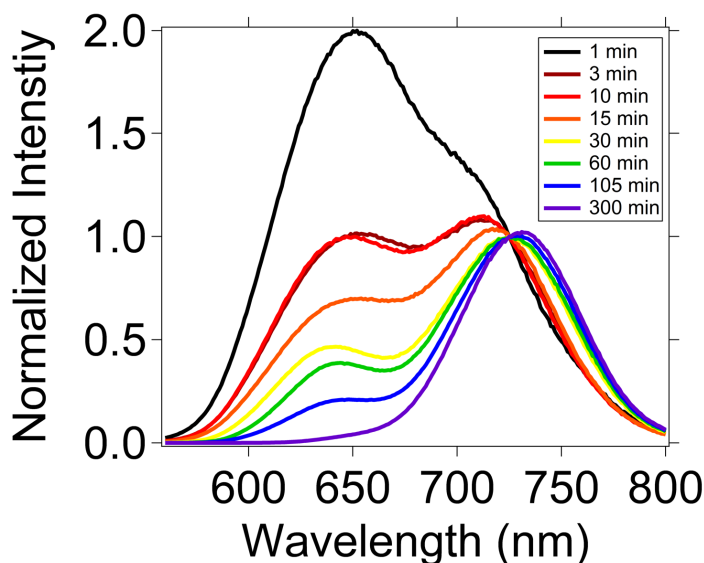


Fig. 5. Flash photolysis luminescence spectra of nanocrystalline $\text{CH}_3\text{NH}_3\text{PbI}_3$ made with Scheme 1 showing thermal relaxation subsequent to laser illumination from a 532-nm, 15-mJ Nd:YAG laser providing nanosecond pulses. Time zero corresponds to the time when the laser was blocked from illuminating the sample.

In order to rule out phase changes as the cause of the photoinduced spectral changes, we conducted *in situ* XRD experiments to search for possible structural changes in the nanocrystalline perovskites during illumination with a pulsed laser. An open window was used to irradiate the samples while they were mounted in the XRD instrument as we have previously reported for other *in situ* XRD measurements [51]. The nanocrystalline material was in the solid state so no solvent effects were present. The $\text{CH}_3\text{NH}_3\text{PbI}_3$ nanocrystalline perovskites exhibited no change in 2θ diffraction peak location or new peaks as a result of irradiation with a laser energy up to 15 mJ (Fig. 6). The *in situ* XRD analysis revealed no additional or shifted diffraction peaks, which indicates that a phase transition does not occur upon illumination.

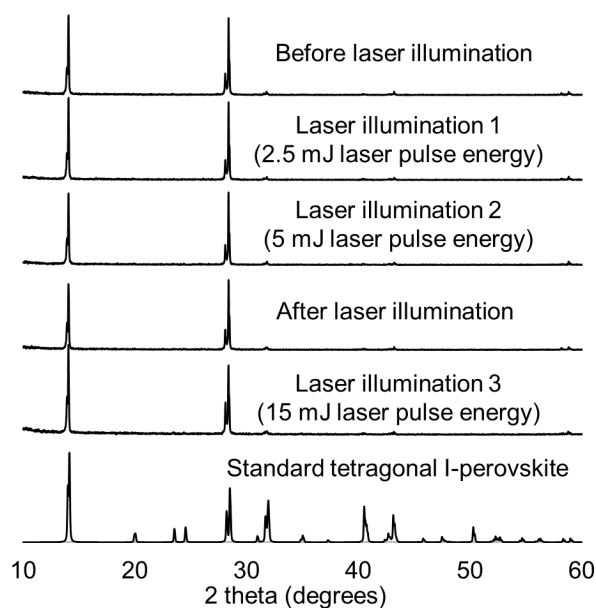
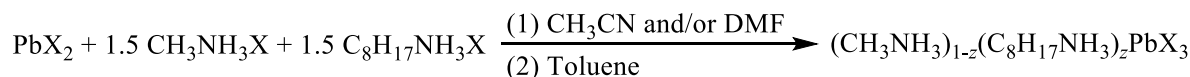


Fig. 6. X-ray diffraction patterns from nanocrystalline $\text{CH}_3\text{NH}_3\text{PbI}_3$ perovskites at different pulse energies. The laser illuminated the sample during the entire time XRD data were collected.

Since a phase change was not measured upon irradiating the sample, the photoinitiated blue photoluminescence peak may result from surface trap states that are populated upon irradiation. In this case, the perovskites have traps with energies above the conduction band that emit at higher energies than the band gap (Fig. 4b inset). An increasing population in trap states with increasing irradiation power could explain the increasing intensity of the 630-nm peak in going from 0.01 mJ to 12 mJ (Fig. 4). Excess precursor may lead to higher energy emissive states which differ from the traditional nanocrystalline lattice expected for $\text{CH}_3\text{NH}_3\text{PbI}_3$ nanocrystals. By using a precursor ratio of 1:1.5:1.5 (Scheme 2), the $\text{CH}_3\text{NH}_3\text{PbBr}_3$ and $\text{CH}_3\text{NH}_3\text{PbI}_3$ exhibited only one luminescence peak at 540 nm and 800 nm, respectively (Fig. 7a, 8a). The disappearance of a second luminescence peak illustrates that bromide and iodide nanocrystalline perovskites prepared using Scheme 2 each have a single emitting state compared to the multiple emitting states observed for the nanocrystals prepared using Scheme 1 with a higher precursor ratio. This observation supports the hypothesis that a synthesis using the smaller ratio of precursors may result in nanocrystals with higher crystalline order and fewer defects compared to a synthesis using a larger precursor ratio.



Scheme 2. Optimized synthesis of nanocrystalline organolead halide ($\text{X} = \text{I}$ or Br) perovskites prepared using a molar concentration of alkylammonium halide precursor that is $1.5\times$ that of the lead halide precursor; $0 < z \ll 1$.

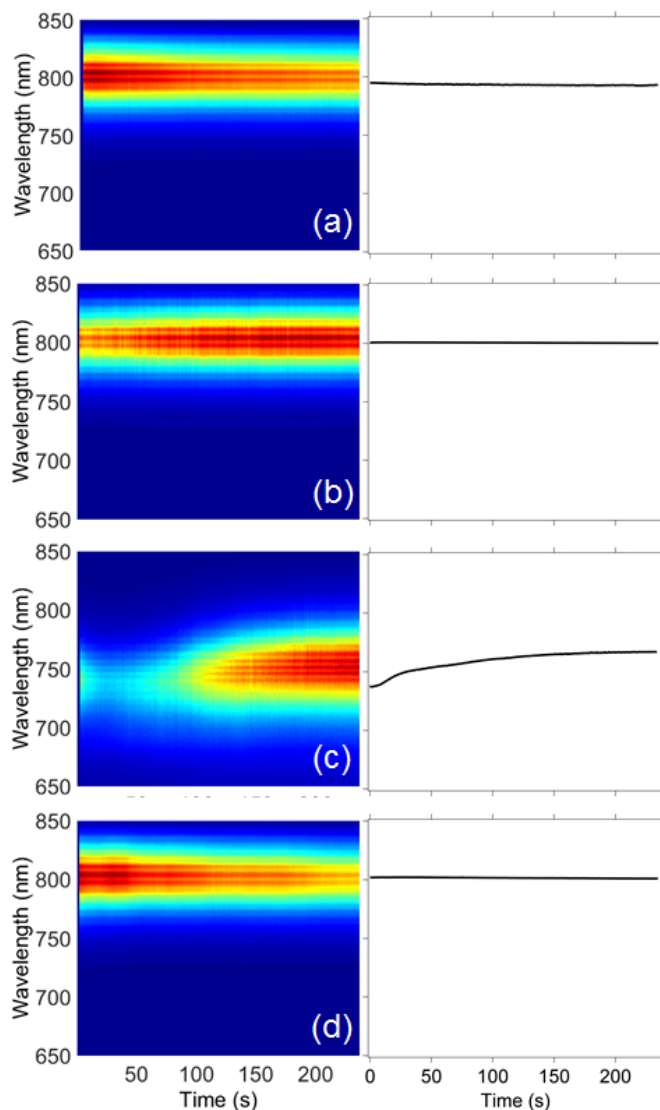


Fig. 7 Time-correlated luminescence microspectroscopy spectra of single $\text{CH}_3\text{NH}_3\text{PbI}_3$ perovskites. The left column shows the plots of luminescence versus illumination time with a 532 nm laser ($1.58 \times 10^5 \text{ W/cm}^2$) for $\text{CH}_3\text{NH}_3\text{PbI}_3$ perovskites synthesized using Scheme 2. The samples are: (a) unwashed sample, (b) washed sample, (c) unwashed with excess precursor, and (d) washed with excess precursor sample. The right column shows the average λ_{max} versus illumination time ($n=3$).

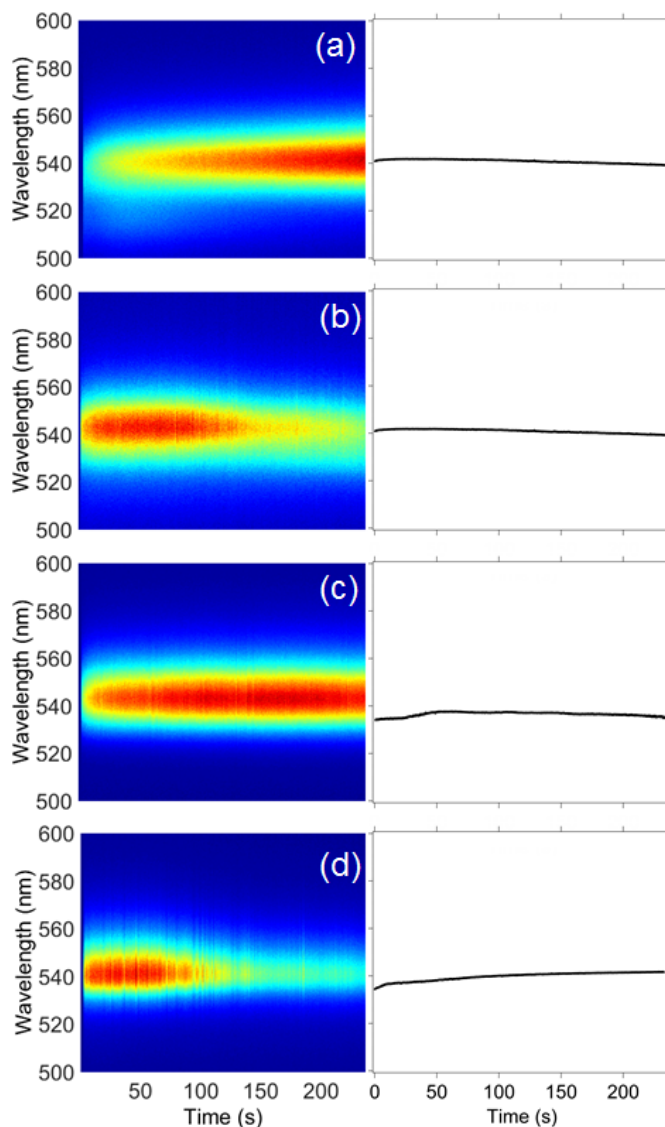


Fig. 8 Time-correlated luminescence microspectroscopy spectra of single $\text{CH}_3\text{NH}_3\text{PbBr}_3$ perovskites. The left column shows the plots of luminescence versus illumination time with a 488 nm laser ($1.58 \times 10^5 \text{ W/cm}^2$) for $\text{CH}_3\text{NH}_3\text{PbBr}_3$ perovskites synthesized using Scheme 2. The samples are: (a) unwashed sample, (b) washed sample, (c) unwashed with excess precursor, and (d) washed with excess precursor sample. The right column shows the average λ_{max} versus illumination time ($n=3$).

Any deviations in λ_{max} are less than 4 nm, and can be explained as measurement uncertainty (e.g., minor changes to the focus). Hu et al. measured no shifts in the luminescence λ_{max} for a single CsPbI_3 nanocrystal after 600 s when excited using a pulsed laser at a temperature of 4 K [62]. They reported a resolution-limited peak width of about 200 μeV , but a laser power density was not reported that could be compared to the experimental parameters we used. Rainò et al. also observed a stable luminescence λ_{max} for a mixed halide $\text{CsPb}(\text{Br}/\text{Cl})_3$ nanocrystal measured for 60 s at 6 K using 92 W/cm^2 excitation [63]. Multiple luminescence peaks and a shifting λ_{max} were measured at higher power densities (up to $4.7 \times 10^3 \text{ W/cm}^2$); the

time-correlated luminescence behavior varied from one nanocrystal to another. In our study, nine of the $\text{CH}_3\text{NH}_3\text{PbI}_3$ nanocrystals measured at room temperature exhibited stable time-correlated luminescence at a higher excitation power density than used by Rainò et al., while three showed a <79-nm shift in λ_{max} . Eight of the $\text{CH}_3\text{NH}_3\text{PbBr}_3$ nanocrystals we measured exhibited stable luminescence behavior while four showed a <8-nm shift in λ_{max} .

To examine the stability of perovskites prepared using the optimized synthetic method with prolonged illumination, luminescence microspectroscopy of individual nanocrystals was employed. For this experiment, a batch of 24-hour-aged perovskites in toluene was divided into four samples. One sample was left as is, and is referred to as the “unwashed sample.” The second sample was mixed with additional 0.012-mM alkylammonium halide (*i.e.*, the same concentration as the precursor solution) and was labeled “unwashed with excess precursor.” For the third and fourth samples, the perovskites were precipitated from the product solution and were resuspended in toluene (“washed sample”) or an 0.01- mM alkylammonium halide solution in toluene (“washed with excess precursor sample”).

The $\text{CH}_3\text{NH}_3\text{PbI}_3$ perovskites prepared using Scheme 2 exhibited a constant λ_{max} of 800 nm for all samples except the unwashed sample with excess precursor. For the latter, the λ_{max} shifts from 737 nm at the start of illumination to 767 nm after 240 s of illumination. Thus, for $\text{CH}_3\text{NH}_3\text{PbI}_3$ additional precursor affects the photostability whether it is present during the synthesis or added post synthesis, although the effect varies (*e.g.*, blue-shifted peak versus red-shifted peak). While the λ_{max} is stable for most of the $\text{CH}_3\text{NH}_3\text{PbI}_3$ samples, the luminescence intensity is variable over the measurement period and photobrightening or photobleaching was measured for most of the nanocrystals (Fig. S2). We have previously reported and discussed this behavior [61].

The nanocrystalline $\text{CH}_3\text{NH}_3\text{PbBr}_3$ perovskites prepared using the optimized synthesis (Scheme 2) exhibited a constant luminescence λ_{max} around 540 nm (Fig. 8) for all samples, even when additional precursor was added to the washed nanocrystals. (No shifts of λ_{max} greater than 4 nanometers were measured). Freppon et al. report the emission of these nanocrystals to be 498 nm when measured in toluene [61]. The red shift in λ_{max} measured for the time-correlated luminescence spectra were measured in the dry state, which explains the difference in the λ_{max} for these two studies. The fact that the luminescence λ_{max} does not shift after adding excess precursor to the nanocrystals synthesized with the optimized method indicates that the higher precursor concentration must be present during the synthesis to have an effect on generating the photoinitiated luminescence peaks for $\text{CH}_3\text{NH}_3\text{PbBr}_3$. Photobrightening and photobleaching were also recorded for $\text{CH}_3\text{NH}_3\text{PbBr}_3$ nanocrystals (Fig. S3).

Conclusion

In order to be useful in a variety of applications, nanocrystalline perovskites need to be photostable. The non-optimized organometal halide perovskites show shifts in luminescence λ_{max} and exhibit multiple luminescence peaks when excess alkylammonium precursor is used. The optimized synthetic method produces nanocrystalline methylammonium lead halide particles that are photostable over at least 4 minutes of focused illumination. The mechanism for the improved photostability is likely to be reduced surface traps when low precursor ratios are utilized. This work reports on the photostability of perovskites containing a single halide. Similar synthetic methods may increase the photostability of related perovskites. In the case of mixed-halide perovskite nanocrystals, where domains of heterogeneous halide compositions may exist, the photostability is more complicated. For example, our initial investigation has shown that $\text{CH}_3\text{NH}_3\text{Pb}(\text{Br}_{0.2}\text{I}_{0.8})_3$ nanocrystalline perovskites exhibit an abrupt shift in λ_{max} from 630 nm to 750 nm after a few seconds of illumination followed by a constant λ_{max} with additional illumination (Fig. S4). Under identical conditions, our initial investigations indicate that single-halide perovskites exhibit stable λ_{max} as reported in this work. Thus, the continued study of mixed-halide perovskites should be pursued.

Acknowledgment

This research is supported by the U.S. Department of Energy, Office of Basic Energy Sciences, Division of Chemical Sciences, Geosciences, and Biosciences through the Ames Laboratory. The Ames Laboratory is operated for the U.S. Department of Energy by Iowa State University under Contract No. DE-AC02-07CH11358. We thank Miles Arthur White for assistance with graphics.

References

1. Green, M. A.; Ho-Baillie, A. *ACS Energy Letters*. **2017**, *2*, 822-830
2. Li, Z.; Klein, T. R.; Kim, D. H.; Yang, M.; Berry, J. J.; van Hest, M. F.; Zhu, K. *Nature Reviews Materials*. **2018**, *3*, 18017
3. Sutherland, B. R.; Sargent, E. H. *Nature Photonics*. **2016**, *10*, 295
4. Dong, Q.; Fang, Y.; Shao, Y.; Mulligan, P.; Qiu, J.; Cao, L.; Huang, J. *Science*. **2015**, *347*, 967-970
5. Kojima, A.; Teshima, K.; Shirai, Y.; Miyasaka, T. *Journal of the American Chemical Society*. **2009**, *131*, 6050-6051
6. Liu, M.; Johnston, M. B.; Snaith, H. J. *Nature*. **2013**, *501*, 395
7. Burschka, J.; Pellet, N.; Moon, S.-J.; Humphry-Baker, R.; Gao, P.; Nazeeruddin, M. K.; Grätzel, M. *Nature*. **2013**, *499*, 316-319
8. Zhou, H.; Chen, Q.; Li, G.; Luo, S.; Song, T.-b.; Duan, H.-S.; Hong, Z.; You, J.; Liu, Y.; Yang, Y. *Science*. **2014**, *345*, 542-546
9. Yang, W. S.; Noh, J. H.; Jeon, N. J.; Kim, Y. C.; Ryu, S.; Seo, J.; Seok, S. I. *Science*. **2015**, *348*, 1234-1237
10. Yang, W. S.; Park, B.-W.; Jung, E. H.; Jeon, N. J.; Kim, Y. C.; Lee, D. U.; Shin, S. S.; Seo, J.; Kim, E. K.; Noh, J. H. *Science*. **2017**, *356*, 1376-1379
11. Christians, J. A.; Miranda Herrera, P. A.; Kamat, P. V. *Journal of the American Chemical Society*. **2015**, *137*, 1530-1538
12. Bert, C.; Jeroen, D.; Nicolas, G.; Aslihan, B.; Jan, D. H.; Lien, D. O.; Anitha, E.; Jo, V.; Jean, M.; Edoardo, M.; De, A. F.; Hans-Gerd, B. *Advanced Energy Materials*. **2015**, *5*, 1500477
13. Berhe, T. A.; Su, W.-N.; Chen, C.-H.; Pan, C.-J.; Cheng, J.-H.; Chen, H.-M.; Tsai, M.-C.; Chen, L.-Y.; Dubale, A. A.; Hwang, B.-J. *Energy & Environmental Science*. **2016**, *9*, 323-356
14. Samrana, K.; Khaja, N. M.; Michael, G.; Shahzada, A. *Angewandte Chemie International Edition*. **2014**, *53*, 2812-2824
15. Gao, P.; Grätzel, M.; Nazeeruddin, M. K. *Energy & Environmental Science*. **2014**, *7*, 2448-2463
16. Dou, L.; Wong, A. B.; Yu, Y.; Lai, M.; Kornienko, N.; Eaton, S. W.; Fu, A.; Bischak, C. G.; Ma, J.; Ding, T. *Science*. **2015**, *349*, 1518-1521
17. Boix, P. P.; Agarwala, S.; Koh, T. M.; Mathews, N.; Mhaisalkar, S. G. *The Journal of Physical Chemistry Letters*. **2015**, *6*, 898-907
18. Sichert, J. A.; Tong, Y.; Mutz, N.; Vollmer, M.; Fischer, S.; Milowska, K. Z.; García Cortadella, R.; Nickel, B.; Cardenas-Daw, C.; Stolarczyk, J. K. *Nano Letters*. **2015**, *15*, 6521-6527
19. Protesescu, L.; Yakunin, S.; Bodnarchuk, M. I.; Krieg, F.; Caputo, R.; Hendon, C. H.; Yang, R. X.; Walsh, A.; Kovalenko, M. V. *Nano Letters*. **2015**, *15*, 3692-3696
20. Deschler, F.; Price, M.; Pathak, S.; Klintberg, L. E.; Jarausch, D.-D.; Higler, R.; Hüttner, S.; Leijtens, T.; Stranks, S. D.; Snaith, H. J.; Ataç, M.; Phillips, R. T.; Friend, R. H. *The Journal of Physical Chemistry Letters*. **2014**, *5*, 1421-1426
21. Zhang, F.; Zhong, H.; Chen, C.; Wu, X.-g.; Hu, X.; Huang, H.; Han, J.; Zou, B.; Dong, Y. *ACS Nano*. **2015**, *9*, 4533-4542
22. Zhu, F.; Men, L.; Guo, Y.; Zhu, Q.; Bhattacharjee, U.; Goodwin, P. M.; Petrich, J. W.; Smith, E. A.; Vela, J. *ACS Nano*. **2015**, *9*, 2948-2959
23. Yang, Z.; Zhang, W.-H. *Chinese Journal of Catalysis*. **2014**, *35*, 983-988

24. Stranks, S. D.; Nayak, P. K.; Zhang, W.; Stergiopoulos, T.; Snaith, H. J. *Angewandte Chemie International Edition*. **2015**, *54*, 3240–3248
25. Yan, K.; Long, M.; Zhang, T.; Wei, Z.; Chen, H.; Yang, S.; Xu, J. *Journal of the American Chemical Society*. **2015**, *137* (13), 4460–4468
26. Tan, Z.-K.; Moghaddam, R. S.; Lai, M. L.; Docampo, P.; Higler, R.; Deschler, F.; Price, M.; Sadhanala, A.; Pazos, L. M.; Credgington, D.; Hanusch, F.; Bein, T.; Snaith, H. J.; Friend, R. H. *Nature Nanotechnology*. **2014**, *9*, 687–692
27. Zhang, M.; Yu, H.; Lyu, M.; Wang, Q.; Yun, J.-H.; Wang, L. *Chemical Communications*. **2014**, *50*, 11727–11730
28. Jang, D. M.; Park, K.; Kim, D. H.; Park, J.; Shojaei, F.; Kang, H. S.; Ahn, J.-P.; Lee, J. W.; Song, J. K. *Nano Letters*. **2015**, *15*, 5191–5199
29. Noh, J. H.; Im, S. H.; Heo, J. H.; Mandal, T. N.; Seok, S. I. *Nano Letters*. **2013**, *13*, 1764–1769
30. Dimesso, L.; Dimamay, M.; Hamburger, M.; Jaegermann, W. *Chemistry of Materials*. **2014**, *26*, 6762–6770
31. Misra, R. K.; Aharon, S.; Li, B.; Mogilyansky, D.; Visoly-Fisher, I.; Etgar, L.; Katz, E. A. *The Journal of Physical Chemistry Letters*. **2014**, 326–330
32. Hoke, E. T.; Slotcavage, D. J.; Dohner, E. R.; Bowring, A. R.; Karunadasa, H. I.; McGehee, M. D. *Chemical Science*. **2015**, *6*, 613–617
33. Sadhanala, A.; Deschler, F.; Thomas, T. H.; Dutton, S. E.; Goedel, K. C.; Hanusch, F. C.; Lai, M. L.; Steiner, U.; Bein, T.; Docampo, P.; Cahen, D.; Friend, R. H. *The Journal of Physical Chemistry Letters*. **2014**, *5*, 2501–2505
34. Gottesman, R.; Gouda, L.; Kalanoor, B. S.; Haltzi, E.; Tirosh, S.; Rosh-Hodesh, E.; Tischler, Y.; Zaban, A.; Quarti, C.; Mosconi, E. *The Journal of Physical Chemistry Letters*. **2015**, *6*, 2332–2338
35. Shao, Y.; Xiao, Z.; Bi, C.; Yuan, Y.; Huang, J. *Nature Communications*. **2014**, *5*, 5784
36. Yuan, Y.; Huang, J. *Accounts of Chemical Research*. **2016**, *49*, 286–293
37. Stranks, S. D.; Burlakov, V. M.; Leijtens, T.; Ball, J. M.; Goriely, A.; Snaith, H. J. *Physical Review Applied*. **2014**, *2*, 034007
38. Wu, X.; Trinh, M. T.; Niesner, D.; Zhu, H.; Norman, Z.; Owen, J. S.; Yaffe, O.; Kudisch, B. J.; Zhu, X.-Y. *Journal of the American Chemical Society*. **2015**, *137*, 2089–2096
39. Wehrenfennig, C.; Liu, M.; Snaith, H. J.; Johnston, M. B.; Herz, L. M. *The Journal of Physical Chemistry Letters*. **2014**, *5*, 1300–1306
40. Lee, M. M.; Teuscher, J.; Miyasaka, T.; Murakami, T. N.; Snaith, H. J. *Science*. **2012**, *338*, 643–647
41. Agiorgousis, M. L.; Sun, Y.-Y.; Zeng, H.; Zhang, S. *Journal of the American Chemical Society*. **2014**, *136*, 14570–14575
42. Sangni, W.; Furong, H.; Liya, Z.; Jianwu, W.; Youling, X.; Peng, J.; Zhuo, C.; Zuodong, Y.; Qi, P.; Zhong, Z. J. *ChemNanoMat*. **2018**, *4*, 409–416
43. Yin, W.-J.; Shi, T.; Yan, Y. *Applied Physics Letters*. **2014**, *104*, 063903
44. Wan-Jian, Y.; Tingting, S.; Yanfa, Y. *Advanced Materials*. **2014**, *26*, 4653–4658
45. Kim, J.; Lee, S.-H.; Lee, J. H.; Hong, K.-H. *The Journal of Physical Chemistry Letters*. **2014**, *5*, 1312–1317
46. Shi, T.; Yin, W.-J.; Hong, F.; Zhu, K.; Yan, Y. *Applied Physics Letters*. **2015**, *106*, 103902
47. Buin, A.; Pietsch, P.; Xu, J.; Voznyy, O.; Ip, A. H.; Comin, R.; Sargent, E. H. *Nano Letters*. **2014**, *14*, 6281–6286
48. Abate, A.; Saliba, M.; Hollman, D. J.; Stranks, S. D.; Wojciechowski, K.; Avolio, R.; Grancini, G.; Petrozza, A.; Snaith, H. J. *Nano Letters*. **2014**, *14*, 3247–3254
49. Noel, N. K.; Abate, A.; Stranks, S. D.; Parrott, E. S.; Burlakov, V. M.; Goriely, A.; Snaith, H. J. *ACS Nano*. **2014**, *8*, 9815–9821
50. Xu, J.; Buin, A.; Ip, A. H.; Li, W.; Voznyy, O.; Comin, R.; Yuan, M.; Jeon, S.; Ning, Z.; McDowell, J. J. *Nature Communications*. **2015**, *6*, 7081
51. Bhattacharjee, U.; Freppon, D.; Men, L.; Vela, J.; Smith, E. A.; Petrich, J. W. *ChemPhysChem*. **2017**, *18* (18), 2526–2532
52. Grabolle, M.; Spieles, M.; Lesnyak, V.; Gaponik, N.; Eychmüller, A.; Resch-Genger, U. *Analytical Chemistry*. **2009**, *81*, 6285–6294

53. Schmidt, L. C.; Pertegás, A.; González-Carrero, S.; Malinkiewicz, O.; Agouram, S.; Mínguez Espallargas, G.; Bolink, H. J.; Galian, R. E.; Pérez-Prieto, J. *Journal of the American Chemical Society*. **2014**, *136*, 850-853
54. De Roo, J.; Ibáñez, M.; Geiregat, P.; Nedelcu, G.; Walravens, W.; Maes, J.; Martins, J. C.; Van Driessche, I.; Kovalenko, M. V.; Hens, Z. *ACS Nano*. **2016**, *10*, 2071-2081
55. Yoon, S. J.; Stamplecoskie, K. G.; Kamat, P. V. *The Journal of Physical Chemistry Letters*. **2016**, *7*, 1368-1373
56. Rosales, B. A.; Hanrahan, M. P.; Boote, B. W.; Rossini, A. J.; Smith, E. A.; Vela, J. *ACS Energy Letters*. **2017**, *2*, 906-914
57. Fedeli, P.; Gazza, F.; Calestani, D.; Ferro, P.; Besagni, T.; Zappettini, A.; Calestani, G.; Marchi, E.; Ceroni, P.; Mosca, R. *The Journal of Physical Chemistry C*. **2015**, *119*, 21304-21313
58. Tanaka, K.; Takahashi, T.; Ban, T.; Kondo, T.; Uchida, K.; Miura, N. *Solid State Communications*. **2003**, *127*, 619-623
59. Pellet, N.; Teuscher, J.; Maier, J.; Grätzel, M. *Chemistry of Materials*. **2015**, *27*, 2181-2188
60. Stranks, S. D.; Eperon, G. E.; Grancini, G.; Menelaou, C.; Alcocer, M. J. P.; Leijtens, T.; Herz, L. M.; Petrozza, A.; Snaith, H. J. *Science*. **2013**, *342*, 341-344
61. Freppon, D. J.; Men, L.; Burkhov, S. J.; Petrich, J. W.; Vela, J.; Smith, E. A. *Journal of Materials Chemistry C*. **2017**, *5*, 118-126
62. Hu, F., Yin, C., Zhang, H., Sun, C., Yu, W.W., Zhang, C., Wang, X., Zhang, Y. and Xiao, M., *Nano Letters*. **2016**. 16(10), 6425-6430
63. Rainò, G., Nedelcu, G., Protesescu, L., Bodnarchuk, M.I., Kovalenko, M.V., Mahrt, R.F., Stöferle, T. *ACS Nano*. **2016** 10(2), 2485-2490.